Proceedings of the
Annual Stability Conference
Structural Stability Research Council
St. Louis, Missouri, April 2-5, 2019

Local buckling of RHS members with small-to-large corner radii subject to combinations of axial force and biaxial bending

Luís Vieira[1], Rodrigo Gonçalves[2], Dinar Camotim[3]

Abstract

This paper presents an in-depth study on the critical local buckling behavior of thin-walled rectangular hollow section (RHS) members subjected to combined axial load and biaxial bending, which accounts for the influence of web-flange interaction and small-to-large corner radii. The calculation of the half-wavelength leading to the minimum critical bifurcation load is performed by means of a Generalized Beam Theory specialization, developed taking advantage of the assumption that the stress resultants are uniform along the member length. This assumption makes it possible to obtain semi-analytical solutions, adopting half-wave sinusoidal amplitude functions for the GBT cross-section deformation modes, and leads to an implementation that (i) is able to quickly solve a large number of cases and (ii) provides physical insight into the critical buckling mode mechanics, through a shell-like stress resultant-based energy criterion, as well as the modal decomposition features of the GBT semi-analytical solution. The critical buckling coefficients obtained in this work are compared with those provided by available analytical expressions and/or currently included in steel design codes, namely Eurocode 3 and the North American Specification for Cold-Formed Steel Members.

1. Introduction

A study concerning the local (plate-like) buckling behavior of rectangular hollow sections (RHS) members was carried out by the authors in the framework of the Research Fund for Coal and Steel project RFCS-2015-709892 – "Overall-Slenderness Based Direct Design for Strength and Stability of Innovative Hollow Sections – HOLLOSSTAB". This study is motivated by the fact that Part 1-5 of the current Eurocode 3 (EC3-1-5 – CEN 2006a) adopts a design approach against local buckling based on the effective width concept and employing expressions developed under the assumption that all cross-section walls are hinged along their internal longitudinal edges – *i.e.*, that each wall may buckle independently from the remaining ones. Although this assumption is on the safe side, since the beneficial effects of the rotational restraints provided by the adjacent walls is discarded, it may constitute a very conservative approach in some cases. Previous work by the authors (Vieira *et al.* 2018) addressed this effect in the context of "straight-edge RHS members", *i.e.*, RHS members without rounded corners. Charts and closed-form formulae were developed for a wide range of loading cases (covering

[1] PhD Student, CERIS, Instituto Superior Técnico, Universidade de Lisboa, <luisjfvieira@tecnico.ulisboa.pt>
[2] Associate Professor, CERIS, Faculdade de Ciências e Tecnologia, Universidade NOVA de Lisboa, <rodrigo.goncalves@fct.unl.pt>
[3] Full Professor, CERIS, Instituto Superior Técnico, Universidade de Lisboa, <dcamotim@civil.ist.utl.pt>

combinations of axial force and biaxial bending), making it possible to calculate web (k_w) and flange (k_f) critical local buckling coefficients, related to the corresponding critical stresses by means of

$$\sigma_{cr}=k_w \frac{\pi^2 E}{12(1-\nu^2)}\left(\frac{t}{h_w}\right)^2 = k_f \frac{\pi^2 E}{12(1-\nu^2)}\left(\frac{t}{b_f}\right)^2 \quad , \quad (1)$$

where σ_{cr} is the local critical stress, E is Young's Modulus, ν is Poisson's ratio, h_w and b_f are the web height and flange width, respectively, and t is the wall thickness. As expected, these coefficients were found to be highly dependent on the (i) cross-section height-to-width ratio (h_w / b_f) and (ii) member loading (or cross-section stress distribution).

Besides the adjacent wall rotation restraint effect, it is also necessary to take into account the influence of the rounded corners, which can lead to significant critical local buckling stress increases. Regarding this influence, it is worth noting that Marsh (1997) investigated the effect of rounded corners on the torsional buckling of angle members and local buckling of square hollow section (SHS) members. In the latter case, an analytical solution was derived under the assumption that the buckling mode consists of single half-waves along the longitudinal and transverse directions. More recently, Zeinoddini & Schafer (2010) investigated the influence of the corner radii on the local strength of cold-formed steel members, by means of shell finite element analyses. They showed that using the Effective Width Method, based on the flat wall widths (as prescribed in the North American Specification for the Design of Cold-Formed Steel Structural Members – AISI 2016)), may lead to unsafe designs. This finding led to the inclusion, in the Commentary to AISI (2016), of a "reduced *k* method", proposed by Robert Glauz[4] and shown to be more accurate, even for r/t values as high as 20 (r is the corner radius). According to this method, the reduced buckling coefficient, termed k_R, is given by

$$k_R=\left(1.08\text{-}0.02\frac{r_1}{t}\right)\left(1.08\text{-}0.02\frac{r_2}{t}\right)k \le k \quad , \quad (2)$$

where r_1 and r_2 are the corner radii and k is calculated on the basis of the wall flat width. However, as noted by Zeinoddini & Schafer (2010), this method does not account for the influence of the b/t ratio and, therefore, may also lead to unsafe designs.

This work is intended (i) to provide an overview of the main findings reported by Vieira *et al.* (2018), namely the easy-to-use charts and closed-form analytical expressions to calculate local buckling coefficients of straight-edge RHS members subjected to a wide range of loadings, and (ii) to extend the previous investigation by accounting for the influence of the rounded corners on the RHS member local buckling behavior. Significant attention is paid to fairly small corner radii, which are those more commonly found in commercial cross-sections – nevertheless, some new findings concerning RHS cross-section members with medium-to-large corner radii are also reported.

The local buckling analyses are performed using a numerical model based on a specialization of Generalized Beam Theory (GBT) for RHS members with or without rounded corners. Originally due to Schardt (1989), GBT is a thin-walled bar theory that handles cross-section in-plane and out-of-plane deformation and is based on expressing the cross-section displacements into a linear combination of "cross-section deformation modes", whose longitudinal amplitude functions constitute the unknowns of the structural problem under consideration (buckling analysis, in this case). GBT is both an efficient and an elegant approach to the structural analysis of prismatic thin-walled members and

[4] The authors learned about this work through its reference made by Zeinoddini & Schafer (2010) – the efforts to find a publication by Robert Glauz bore no fruits.

structural systems, due to its ability (i) to provide accurate and structurally enlightening solutions with just a few deformation modes and also (ii) to include or exclude specific effects in a very straightforward manner. A detailed account of the fundamentals, capabilities and applications of GBT can be found in the list of publications on GBT by the "Lisbon GBT research group", available at *www.civil.ist.utl.pt/gbt* – moreover, a user-friendly computer program to perform GBT-based buckling and vibration analyses of thin-walled members (Bebiano *et al.* 2018) can be downloaded in this website.

The outline of the paper is as follows. Section 2 describes the GBT-based numerical model developed to calculate the critical local bifurcation stresses. In Section 3, parametric studies are conducted for straight-edge RHS members subjected to both simple and complex loadings, including combinations of axial force and biaxial bending. They aim at investigating the influence of the height-to-width and height-to-thickness ratios on the RHS member local buckling behavior, and also at assessing the importance of including "non-Vlasov local deformation modes" in the GBT analyses. The results obtained are compared with values currently available in the literature, and also used to plot charts and develop approximate analytical formulae to calculate local buckling coefficients. Section 4 addresses the influence of the rounded corners for RHS members subjected to several combinations of axial force and biaxial bending. In particular, equivalent local buckling coefficients are proposed for members with rounded corners, which are subsequently used to develop expressions providing correction coefficients that accurately take into account the rounded corner influence. Moreover, a preliminary study, concerning SHS (square hollow section) members with increasing corner radii, up to the circular tube case, is presented and discussed. Finally, Section 5 summarizes the main conclusions of the work.

2. GBT-Based Numerical Model

The numerical model adopted in this work is based on a GBT specialization specifically developed to calculate critical local bifurcation stresses of RHS members subjected to longitudinally uniform stress combinations. After identifying the relevant cross-section deformation modes, the computation of the critical local bifurcation loadings is addressed – GBT-based semi-analytical analyses are employed to perform this task.

2.1 Cross-Section Deformation Modes

The RHS rounded-edge and straight-edge configurations considered in this work have geometries defined by the parameters shown in Figure 1(a). The cross-section global axes are denoted Y and Z, and coincide with the major and minor bending axes, respectively. The cross-section is discretized by subdividing each cross-section element (web, flange or corner) into equal-length straight walls, as illustrated in Figure 1(b): two intermediate nodes per web, one intermediate node per flange, and one intermediate node per corner (rounded-edge RHS only). Since the procedures leading to the deformation modes are identical for rounded-edge and straight-edge RHS, and for the sake of simplicity, the illustration presented next concerns exclusively the straight-edge case. Mid-surface local axes (x, y, z) are defined in each wall, which are associated with the displacement components pertaining to each deformation mode k: $\bar{u}_k$, $\bar{v}_k$ and $\bar{w}_k$, along the longitudinal axis, the cross-section mid-line and the wall thickness, respectively – see Figure 1(c). These modal displacement components are expressed as

$$\begin{aligned} u_k &= \bar{u}_k(y)\phi_{k,x}(x), \\ v_k &= \bar{v}_k(y)\phi_k(x), \\ w_k &= \bar{w}_k(y)\phi_k(x), \end{aligned} \quad , \qquad (3)$$

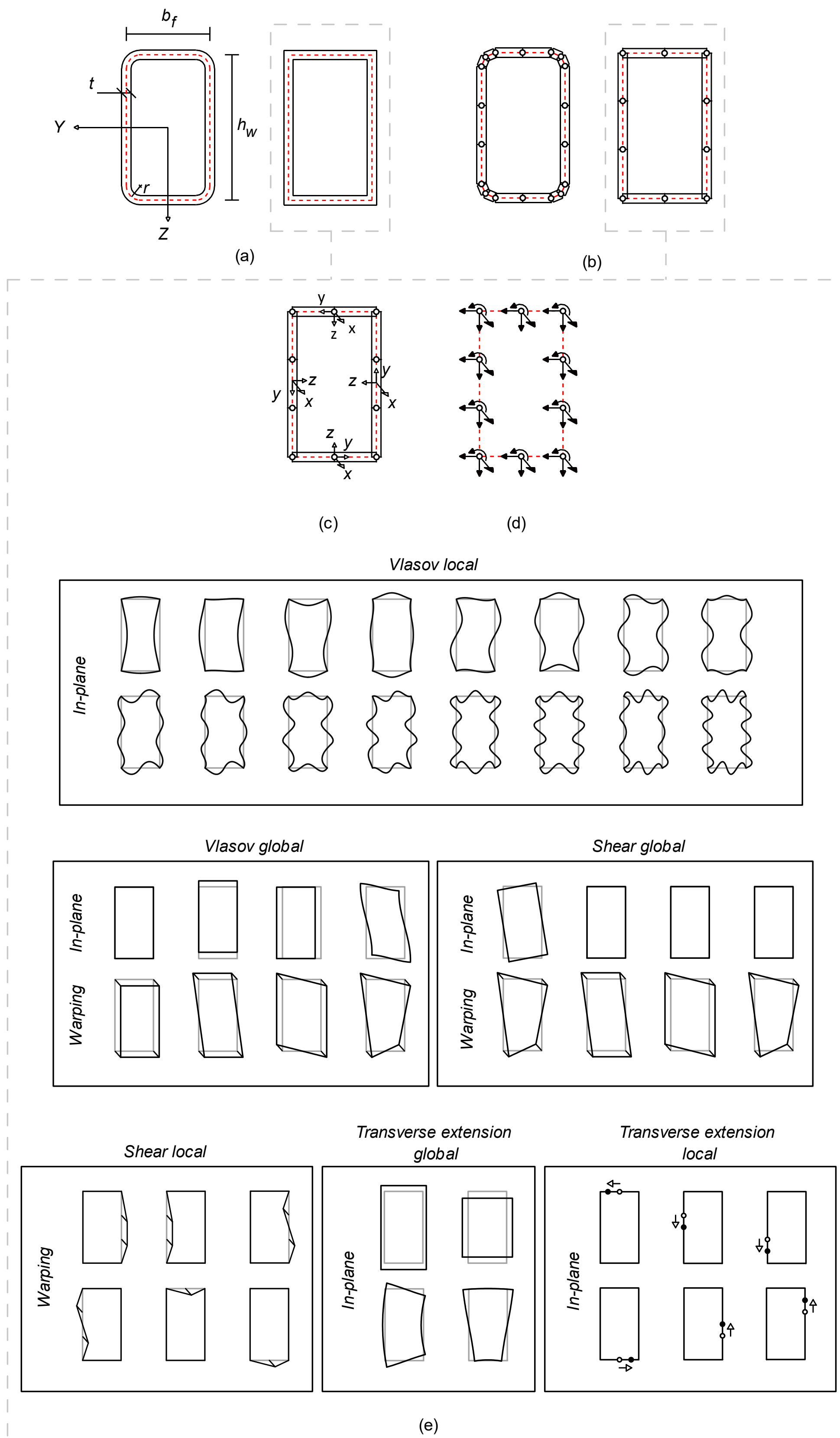

Figure 1: (a) Geometry and (b) discretization of a rounded RHS and its straight-edge equivalent, (c) local axes, (d) imposed unit displacements and rotations, and (e) deformation mode shapes in the equivalent straight-edge RHS

where subscript commas indicate differentiation, $\bar{u}_k(y)$, $\bar{v}_k(y)$, $\bar{w}_k(y)$ are the deformation mode shape functions and $\phi_k(x)$ are the corresponding modal amplitude functions.

An initial deformation mode basis is generated by imposing, at each node, three unit displacements along the local axes and one in-plane unit rotation, as shown in Figure 1(d). This leads to a deformation mode space with $4N$ modes, where N is the total number of nodes. Note that this procedure differs from the classic GBT one, in which the in-plane rotations are statically condensed. The displacement functions $\bar{u}_k$ and $\bar{v}_k$ are approximated by means of Lagrange linear polynomials, whereas Hermite cubic functions are employed to approximate $\bar{w}_k$. The final deformation modes are calculated as explained by Gonçalves *et al.* (2010), through a procedure that only differs from the standard one in the fact that the in-plane nodal rotations are also included. This procedure comprises the solution of a sequence of eigenvalue problems, involving pairs of GBT modal linear and geometric stiffness matrices (see Eqs. (4) and (6) below) – the deformation modes correspond to the eigenvectors yielded by the above successive eigenvalue problems.

The deformation mode shapes, displayed in Figure 1(e), can be subdivided into three distinct groups:

(i) *Vlasov Modes*, associated with null membrane shear strains (Vlasov's assumption) and transverse extensions: four global modes (axial extension, two bending modes and one distortional mode) and several local modes, depending on the cross-section discretization. In the presence of rounded corners the local modes no longer exhibit null in-plane displacements at the wall junctions and, furthermore, they involve warping displacements, as found by Gonçalves & Camotim (2016).

(ii) *Shear Modes*, associated with non-null membrane shear strains: four global modes (torsion and warping displacements corresponding to the Vlasov bending and distortional modes) and several local warping modes, depending on the cross-section discretization.

(iii) *Transverse Extension Modes*, associated with non-null membrane shear strains and transverse extensions: four global modes and several local modes, depending on the cross-section discretization.

In general, the local buckling behavior of RHS members can be accurately assessed by performing GBT analyses including only the Vlasov local modes, even if other deformation have small participations in the solution. Therefore, two GBT buckling analysis variants were employed in this work: "Variant 1", which includes only the Vlasov local modes, and "Variant 2", including all the $4N$ modes. Naturally, Variant 2 is the most accurate and computationally expensive (more so for very fine cross-section discretizations) – moreover, it enables the quantification of the errors involved in the use of Variant 1 (including only the Vlasov local modes).

For Variant 1, a rather fast procedure can be devised to calculate the Vlasov local modes, by using the GBT modal linear stiffness matrices, which read (*e.g.*, Gonçalves *et al*. 2010)

$$
\begin{aligned}
B_{ij} &= B_{ij}^{M}+B_{ij}^{B} = \int_S \frac{Et}{1-\nu^2}\bar{v}_{i,y}\bar{v}_{j,y}\,dy + \int_S \frac{Et^3}{12(1-\nu^2)}\bar{w}_{i,yy}\bar{w}_{j,yy}\,dy\,,\\
C_{ij} &= C_{ij}^{M}+C_{ij}^{B} = \int_S \frac{\alpha Et}{1-\nu^2}\bar{u}_i\bar{u}_j\,dy + \int_S \frac{Et^3}{12(1-\nu^2)}\bar{w}_i\bar{w}_j\,dy\,,\\
D_{1ij} &= D_{1ij}^{M}+D_{1ij}^{B} = \int_S Gt\left(\bar{u}_{i,y}+\bar{v}_i\right)\left(\bar{u}_{j,y}+\bar{v}_j\right)dy + \int_S \frac{Gt^3}{3}\bar{w}_{i,y}\bar{w}_{j,y}dy\,,
\end{aligned}
\qquad (4)
$$

where $(\cdot)^M$ and $(\cdot)^B$ denote the membrane and bending terms, respectively, G is the shear modulus and one has either α=1, if transverse extensions deformation modes are included, or $\alpha = \left(1-\nu^2\right)$, otherwise. This procedure involves the following two steps:

(i) The shear and transverse extension modes are removed by calculating the $2N$ dimension basis of the nullspace of $\left(\mathbf{D}_1^M + \mathbf{B}^M\right)$, which corresponds to the Vlasov modes (null membrane shear strains and transverse extensions).

(ii) The local modes are the eigenvectors associated with the non-null eigenvalues of $\mathbf{B}^B\mathbf{v} = \lambda\mathbf{C}\mathbf{v}$, with the exception of the lowest one, always corresponding to the RHS single distortional mode.

Sinusoidal amplitude functions of the form $\phi_k(x) = \bar{\phi}_k \sin(\pi x/L)$, where L is the half-wave length and $\bar{\phi}_k$ is the mode amplitude, constitute exact solutions for simply supported members and lead to the bifurcation equation (Gonçalves *et al.* 2010)

$$\left(\frac{\pi^2}{L^2}\,\mathbf{C} + \mathbf{D} + \frac{L^2}{\pi^2}\mathbf{B} + \lambda\left(\mathbf{X}_1 + \frac{\pi^2}{L^2}\mathbf{X}_2\right)\right)\bar{\boldsymbol{\phi}} = \mathbf{0} \qquad , \quad (5)$$

where λ is the load parameter and

$$\begin{aligned}
\mathbf{D} &= \mathbf{D}_1 - \mathbf{D}_2 - \mathbf{D}_2^{\mathrm{T}},\\
D_{2_{ij}} &= D_{2ij}^M + D_{2ij}^B = \int_S \frac{vEt}{1-v^2}\,\bar{v}_{i,y}\bar{u}_j\, dy + \int_S \frac{vEt^3}{12\left(1-v^2\right)}\,\bar{w}_{i,yy}\bar{w}_j\, dy,\\
X_{1_{ij}} &= \int_S \sigma\left(\bar{v}_i\bar{v}_j + \bar{w}_i\bar{w}_j\right) dy\,,\\
X_{2_{ij}} &= \int_S \sigma\left(\bar{u}_i\bar{u}_j\right) dy\,,
\end{aligned} \qquad , \quad (6)$$

where $\mathbf{X}_1$ and $\mathbf{X}_2$ are geometric stiffness matrices, $\sigma = \sigma(y)$ is the pre-buckling membrane longitudinal normal stress function, defined along the cross-section mid-line y. The buckling eigenvalue problem defined by Eq. (6) is computationally very efficient, since the DOF number equals the number of deformation modes included in the analysis. However, the calculation of the half-wave length associated with the minimum critical bifurcation load parameter requires an iterative strategy – the golden-section search algorithm was employed (Kiefer 1953). The critical buckling mode shape is obtained from the eigenvector corresponding to the lowest eigenvalue λ, which constitutes the critical load parameter. The linear strain energy U associated with that buckling mode, by means of through

$$U = \frac{1}{2}\int_L \left(\boldsymbol{\phi}_{,\mathrm{xx}}^{\mathrm{T}}\mathbf{C}\boldsymbol{\phi}_{,\mathrm{xx}} + \boldsymbol{\phi}_{,\mathrm{x}}^{\mathrm{T}}\mathbf{D}_1\boldsymbol{\phi}_{,\mathrm{x}} + \boldsymbol{\phi}_{,\mathrm{xx}}^{\mathrm{T}}\mathbf{D}_2\boldsymbol{\phi} + \boldsymbol{\phi}^{\mathrm{T}}\mathbf{B}\boldsymbol{\phi} + \boldsymbol{\phi}^{\mathrm{T}}\mathbf{D}_2{}^{\mathrm{T}}\boldsymbol{\phi}_{,\mathrm{xx}}\right)dx, \qquad , \quad (7)$$

where $\boldsymbol{\phi}$ is a column vector containing the modal amplitude functions. The mechanics involved may be better grasped if the six shell-like components of the above strain energy are inspected separately. They stem for the longitudinal membraneU_x^M, transverse membrane U_y^M, shear membrane U_{xy}^M, longitudinal bending U_x^B, transverse bending U_y^B and shear bending (torsion) U_{xy}^B strains, and read

$$\begin{aligned}
U &= U_x^M + U_y^M + U_{xy}^M + U_x^B + U_y^B + U_{xy}^B,\\
U_x^M &= \frac{1}{2}\int_L \sigma_{\mathrm{xx}}^M\varepsilon_{\mathrm{xx}}^M\, dx = \frac{L}{4}\left(\left(\frac{\pi}{L}\right)^4 \bar{\boldsymbol{\phi}}^{\mathrm{T}}\mathbf{C}^M\bar{\boldsymbol{\phi}} - \left(\frac{\pi}{L}\right)^2 \bar{\boldsymbol{\phi}}^{\mathrm{T}}\mathbf{D}_2^M\bar{\boldsymbol{\phi}}\right),\\
U_y^M &= \frac{1}{2}\int_L \sigma_{yy}^M\varepsilon_{yy}^M\, dx = \frac{L}{4}\left(\bar{\boldsymbol{\phi}}^{\mathrm{T}}\mathbf{B}^M\bar{\boldsymbol{\phi}} - \left(\frac{\pi}{L}\right)^2 \bar{\boldsymbol{\phi}}^{\mathrm{T}}\mathbf{D}_2^{M\,\mathrm{T}}\bar{\boldsymbol{\phi}}\right),\\
U_{xy}^M &= \frac{1}{2}\int_L \sigma_{\mathrm{xy}}^M\varepsilon_{\mathrm{xy}}^M\, dx = \frac{L}{4}\left(\frac{\pi}{L}\right)^2 \bar{\boldsymbol{\phi}}^{\mathrm{T}}\mathbf{D}_1^M\bar{\boldsymbol{\phi}},\\
U_x^B &= \frac{1}{2}\int_L \sigma_{\mathrm{xx}}^B\varepsilon_{\mathrm{xx}}^B\, dx = \frac{L}{4}\left(\left(\frac{\pi}{L}\right)^4 \bar{\boldsymbol{\phi}}^{\mathrm{T}}\mathbf{C}^B\bar{\boldsymbol{\phi}} - \left(\frac{\pi}{L}\right)^2 \bar{\boldsymbol{\phi}}^{\mathrm{T}}\mathbf{D}_2^B\bar{\boldsymbol{\phi}}\right),
\end{aligned} \qquad . \quad (8)$$

$$U_y^B = \frac{1}{2}\int_L \sigma_{yy}^B \varepsilon_{yy}^B \, dx = \frac{L}{4}\left(\overline{\boldsymbol{\Phi}}^{\mathrm{T}} \mathbf{B}^B \overline{\boldsymbol{\Phi}} - \left(\frac{\pi}{L}\right)^2 \overline{\boldsymbol{\Phi}}^{\mathrm{T}} \mathbf{D}_2^{B\,\mathrm{T}} \overline{\boldsymbol{\Phi}}\right),$$

$$U_{xy}^B = \frac{1}{2}\int_L \sigma_{\mathrm{xy}}^B \varepsilon_{\mathrm{xy}}^B \, dx = \frac{L}{4}\left(\frac{\pi}{L}\right)^2 \overline{\boldsymbol{\Phi}}^{\mathrm{T}} \mathbf{D}_1^B \overline{\boldsymbol{\Phi}}.$$

The relative importance of each component may be easily quantified by calculating its ratio with respect to the total strain energy U. Therefore, from the analysis of these ratios for equivalent rounded-edge and straight-edge RHS members, it is possible to unveil the changes in the local buckling mechanics occurring when the rounded corners are taken into account. Finally, one last word to mention that the code was implemented in MATLAB (the MathWorks Inc. 2017) and the numerical integrations along *y* are performed using 4 Gauss points (exact for the approximation functions used).

3. Straight-Edge RHS Members – Overview

A total of 124 RHS members were analysed by Vieira *et al.* (2018), exhibiting h_w/t values comprised between 1 and 4 (with a step of 0.1), and b_f/t values ranging from 10 to 40 (with a step of 10), which covers most standard commercial cross-sections (CEN 2006b). The RHS members were modelled as straight-edge and simplified to their mid-surface, adopting a cross-section discretization involving five segments per wall – previous mesh convergence studies (Vieira *et al.* 2018) showed that this discretization ensures accurate results.

The two numerical model variants addressed in Section 2 (analyses with the Vlasov local modes only or with all the deformation modes) are initially considered – the results obtained were thoroughly validated through the comparison with values provided by GBTUL (Bebiano *et al.* 2018) and CUFSM (Li & Schafer 2010). Table 1 shows the statistical indicators (average, standard deviation, maximum and minimum values) of the differences between the critical local bifurcation coefficients obtained with the two variants for several combinations of axial force and biaxial bending – the indicators concern members sharing the same b_f/t value. Naturally, a critical local buckling stress reduction is observed when all modes are included in the analysis (Variant 2). Moreover, there is a clear correlation between this reduction and the b_f/t ratio – noteworthy differences are obtained for b_f/t=10 only, *i.e.*, for members with rather stocky cross-sections. For b_f/t values higher than 10, the results provided by Variant 1 are very accurate, as reflected by difference averages below 1% and very small standard deviations. Therefore, it is perfectly acceptable to use Variant 1 to analyze the RHS member local buckling behavior. Moreover, the local buckling coefficients become independent of the b_f/t ratio, a very relevant feature – then, these coefficients depend only on the (i) stress distribution and (ii) h_w/b_f ratio.

Table 1: Statistical indicators of the differences between the critical local buckling coefficients obtained with Variants 2 and 1

	$\frac{b_f}{t} = 10$	$\frac{b_f}{t} = 20$	$\frac{b_f}{t} = 30$	$\frac{b_f}{t} = 40$
Average	-2.9%	-0.7%	-0.3%	-0.2%
Standard Deviation	1.4%	0.3%	0.2%	0.1%
Minimum	-11.1%	-2.5%	-1.1%	-0.6%
Maximum	-0.1%	-0.0%	-0.1%	-0.0%

The influence of the h_w/b_f ratio on the local buckling coefficient is investigated in Section 3.1 for simple loadings (axial compression, major and minor-axis bending), in which case the results obtained can be compared with values available in the literature. The loading cases combining axial force and biaxial bending are addressed in Section 3.2 – due to space limitations, the results presented concern only members with h_w/b_f=1, 2, 3, 4 (the full set of results can be found in Vieira *et al.* 2018). Finally, Section 3.3 presents charts and analytical expressions to determine local buckling coefficients.

3.2 Local Buckling under Simple Loadings

Figures 2 to 4 show plots that provide the variation of the web and flange buckling coefficients with the h_w/b_f ratio, for RHS members subjected to axial compression, minor-axis bending and major-axis bending – the figures also display various buckling modes, scaled to exhibit the same web maximum displacement. The results concerning axial compression (Fig. 2) coincide with those reported by Stowell & Lundquist (1939) and differ slightly from those yielded by the analytical expressions developed by Seif & Schafer (2010). As for the local buckling coefficients concerning major-axis and minor-axis bending (Figs. 3 and 4, respectively), the values provided by the GBT-based numerical model are very similar to those obtained by Seif & Schafer (2010).

The influence of h_w/b_f on k_w and k_f visibly depends on the stress distribution. For an axially compressed square tube, all walls are identical and uniformly compressed and, therefore, one has necessarily k_w=k_f=4.0 (value concerning simply supported square plates). As h_w/b_f increases beyond 1.0 (*i.e.*, web-driven local buckling), the web end rotations become increasingly restrained by the flanges, leading to a k_w increase and, necessarily (see Eq. (1)), a k_f decrease. For minor-axis bending, one web is uniformly compressed and the flanges are under an anti-symmetric linear stress diagram. Since buckling is practically always driven by the compressed web, the h_w/b_f ratio has a minute influence on k_w. For major-axis bending, the compressed flange governs the local buckling behaviour if h_w/b_f≈1.0 (*i.e.*, sections close to SHS) and, therefore, the variation of k_f is very weak. However, if h_w/b_f considerably exceeds 1.0, local buckling is driven by the web (under linear compression) and a k_f reduction takes place.

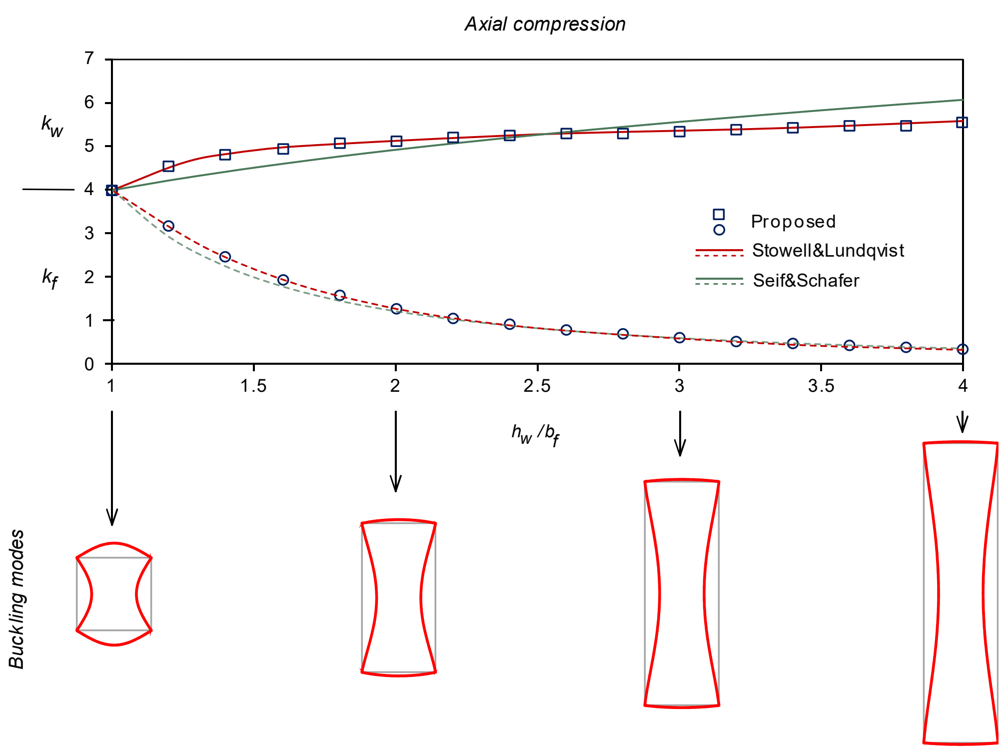

Figure 2: Local buckling coefficients and buckling mode shapes for RHS members under axial compression

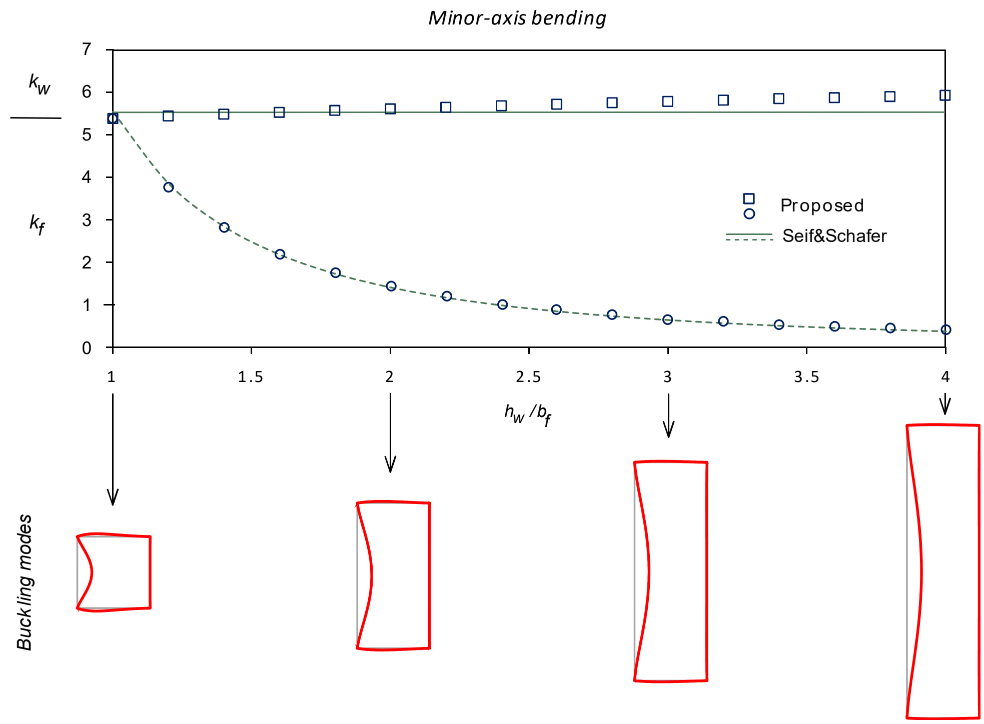

Figure 3: Local buckling coefficients and buckling mode shapes for RHS members under minor-axis bending

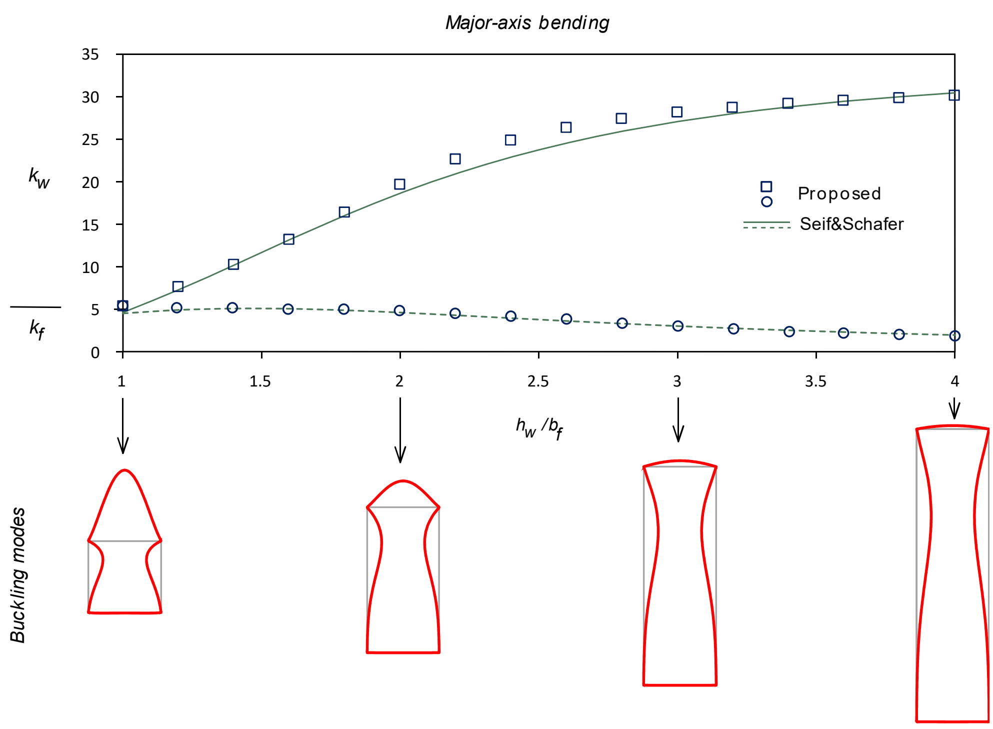

Figure 4: Local buckling coefficients and buckling mode shapes for RHS members under major-axis bending

As expected, it is concluded that buckling tends to be governed by the webs as h_w/b_f increases. Moreover, for a given loading (stress distribution), an h_w/b_f increase causes an increase in the relation between the web and flange compressed widths, which automatically implies that the flanges provide more restraint to the web end rotations.

3.2 Local Buckling under Combined Axial Force and Biaxial Bending

For combined loading, an arbitrary loading (stress distribution – see Fig. 5(a)) may be parameterized through parameters defined by

$$\Psi_w = \frac{\sigma_B}{\sigma_A}, \qquad \Psi_f = \frac{\sigma_C}{\sigma_A}, \qquad (9)$$

where Ψ_w and Ψ_f are comprised between –1.0 and 1.0 (in this work) and point A stands for the most compressed web-flange mid-line corner (in this work, the wider RHS cross-section walls are always termed "webs") – points B and C are the far web and flange ends, respectively. Figure 5(b) identifies, in the Ψ_w- Ψ_f 2D space, the simple and combined loading cases – while the former have already been addressed in Section 3.1, the latter are omitted from this work due to space limitations (the results can be found in Vieira *et al.* 2018). Finally, note that $\Psi_w < -\Psi_f$ means that the cross-section is under axial tension.

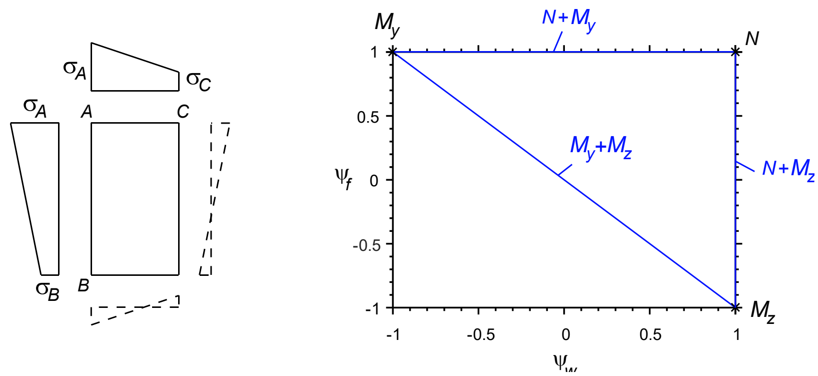

(a) (b)

Figure 5: (a) Arbitrary normal stress distribution in a RHS under combined axial force and biaxial bending, and (b) identification of the load combinations considered in the Ψ_w- Ψ_f 2D space

In order to enable a better understanding on how the stress distribution profile is related to the critical local buckling, and given the fact that the RHS member instability is almost always driven by the webs, only k_w is referred from her onwards – of course, k_f may be easily retrieved from Eq. (1).

Figure 6 shows the web buckling coefficients obtained for different h_w/b_f ratios, displayed as Ψ_w- Ψ_f surface plots and corresponding isolines. Both the surface plots and isolines have been obtained, by means of curve-fitting techniques, from the web buckling coefficients obtained for (Ψ_w, Ψ_f) pairs defining a mesh with 0.1 intervals along both axes – the MATLAB *griddata* method with bi-harmonic spline interpolation was employed. It is readily observed that, in agreement with the previous findings, the buckling coefficient increases as Ψ_w and/or Ψ_f decreases. For SHS, the surfaces are naturally symmetric with respect to the $\Psi_w = \Psi_f$ axis and, for increasingly narrower RHS, they become mostly dependent on Ψ_w. This transition agrees with the gradual shift of the maximum biaxial bending k_w value towards lower Ψ_w ratios (see also Fig. 10). Finally, note also that, even for the highest h_w/b_f value considered, k_w decreases as Ψ_f approaches 1.

3.3 Approximate Formulae

On the basis of the results obtained previously it is possible to develop approximate analytical formulae to calculate local buckling coefficients of RHS members under combined axial force and biaxial bending. The weighted linear least squares method was used, employing increasingly higher-order polynomials until correlation was deemed satisfactory. Instead of using Ψ_w and Ψ_f directly as input

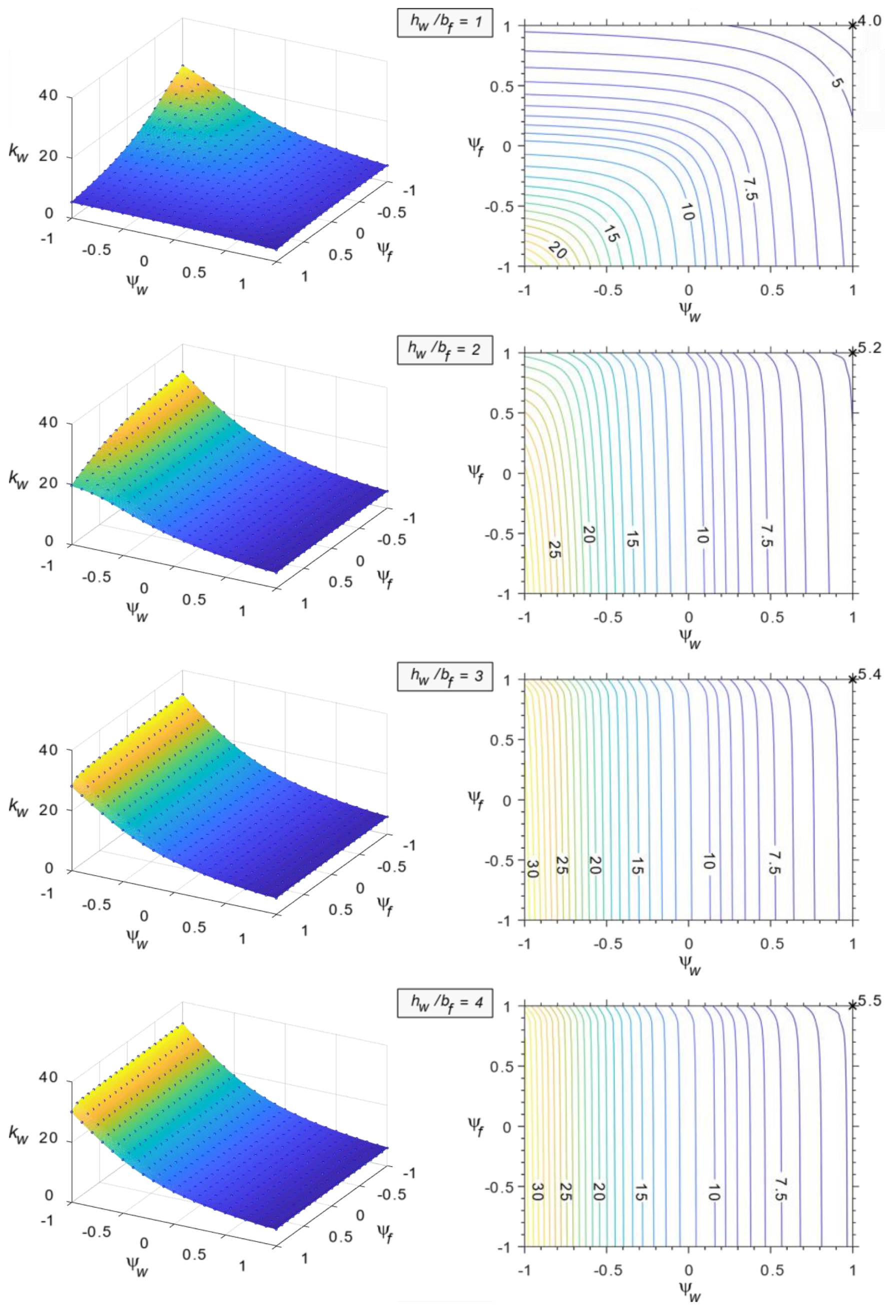

Figure 6: Buckling coefficient (k_w) surface plots and contour lines of RHS members under axial force and biaxial bending

parameters, shifted coordinates $\Psi'_w = \Psi_w - 1$ and $\Psi'_f = \Psi_f - 1$ are adopted – this choice considerably simplifies the polynomials obtained. Table 2 displays the formulae proposed to calculate k_w and Table 3 provides their coefficients as functions of the h_w/b_f ratio. Note that the main and cross-order coefficients are of the 4th and 5th degree, respectively, and that $p_{00}=k_w$ for uniformly compressed RHS members.

4. Rounded-Edge RHS Members – Influence of the Corner Radii

This section aims at investigating the influence of the explicit consideration of the rounded corners on the local buckling behavior of RHS members subjected to combinations of axial force and biaxial

Table 2: Analytical formulae to calculate k_w in RHS members subjected to various loading cases

N-M_y-M_z	$p_{00}+\sum_{i=1}^{4}\left(p_{i0}(\psi_w-1)^i+p_{0i}(\psi_f-1)^i\right)+\sum_{i=1}^{4}\sum_{j=1}^{5-i}p_{ij}(\psi_w-1)^i(\psi_f-1)^j$
N	p_{00}
N-M_y	$p_{00}+\sum_{i=1}^{4}p_{i0}(\psi_w-1)^i$
N-M_z	$p_{00}+\sum_{i=1}^{4}p_{0i}(\psi_f-1)^i$

Table 3: Coefficients of the polynomial developed to calculate the local buckling coefficients k_w

h_w/b_f	p_{00}	p_{01}	p_{02}	p_{03}	p_{04}	p_{10}	p_{20}	p_{30}	p_{40}	
1	4.000	-2.230	-1.585	-0.543	-0.070	-2.230	-1.585	-0.543	-0.070	
2	5.158	-1.571	-2.396	-1.497	-0.322	-4.488	-6.436	-9.368	-2.727	
3	5.384	-1.554	-2.432	-1.528	-0.329	-3.895	-3.141	-5.076	-0.822	
4	5.541	-1.549	-2.445	-1.540	-0.333	-3.853	-2.577	-4.414	-0.518	
h_w/b_f	p_{11}	p_{21}	p_{12}	p_{31}	p_{22}	p_{13}	p_{41}	p_{32}	p_{23}	p_{14}
1	-1.373	-2.837	-2.837	0.018	-3.005	0.018	0.561	-0.945	-0.945	0.561
2	0.101	-2.660	1.592	-2.906	0.681	0.607	-1.489	0.473	0.141	0.021
3	1.574	-0.847	3.887	-0.081	-1.112	3.343	-0.285	0.323	-0.553	0.928
4	1.575	-0.665	3.816	0.219	-1.127	3.261	-0.081	0.183	-0.463	0.884

bending, namely the changes in (i) the critical buckling stress/coefficients and (ii) the buckling mechanics. These changes are assessed by comparing the GBT-based results obtained for straight-edge and rounded-edge RHS member configurations. In order to facilitate handling the most complex loading cases, for which the maximum stress occurs at the rounded corners, new local buckling coefficients $\overline{k_w}$ and $\overline{k_f}$ are introduced, concerning the (fictitious) critical local buckling stress ($\overline{\sigma_{cr}}$) acting at the most compressed web-flange mid-line intersection (point A in Figure 7a)). Then, this critical local buckling stress is given by

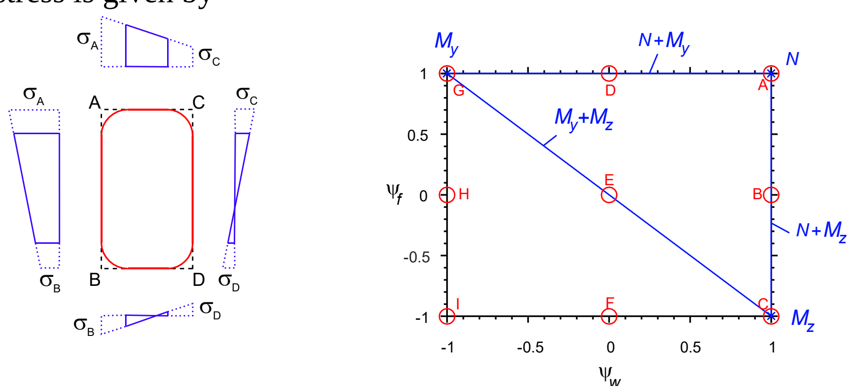

(a) (b)

Figure 7: (a) Stress parameter definition for RHS with rounded corners and (b) identification of the load combinations considered in the Ψ_w- Ψ_f 2D space

$$\overline{\sigma_{cr}}=\overline{k_w}\frac{\pi^2 E}{12(1-\nu^2)}\left(\frac{t}{h_w}\right)^2=\overline{k_f}\frac{\pi^2 E}{12(1-\nu^2)}\left(\frac{t}{b_f}\right)^2 \quad . \quad (10)$$

Naturally, the k_w and k_f values obtained for the straight-edge RHS members are just a particular case of the new buckling coefficients $\overline{k_w}$ and $\overline{k_f}$, obtained when the radii are null. Therefore, the influence of the rounded corners on the RHS member local buckling behaviour may be easily assessed by means of a reduction coefficient $C_{k,r}$, given by

$$C_{k,r}=\frac{\overline{k_w}}{k_{w,str\text{-}edge}}=\frac{\overline{k_f}}{k_{w,str\text{-}edge}} \quad , \quad (11)$$

where subscript "*str-edge*" indicates the same RHS cross-section, but with straight edges.

The first part of this study (Sections 4.1 to 4.5) focuses on the influence of (small) rounded corners on members with RHS geometries commonly used in practice, namely the comprehensive cross-section set specified in the EN10219-Part 2 (CEN 2006b) database. Preliminary mesh sensitivity studies indicated that good accuracy is obtained using 5 wall segments per web, flange and corner, a mesh that was subsequently adopted in all the analyses. For the rounded-edge RHS configurations, the mean radius values were computed in accordance with the above code provisions, which are reproduced in Table 4. However, according to these provisions, some cross-sections have very narrow flat widths and can hardly be considered "thin-walled". Thus, out of the whole set of RHS identified above, those exhibiting walls with flat widths lower than 10 times the thickness are left out – a total of 186 cross-sections (100 SHS and 86 RHS) are considered in this work.

Table 4: EN10219-Part 2 provisions to determine the mean corner radii to be considered

Thickness (t)	External corner radius (r_o)	Internal corner radius (r_i)	Mean corner radius (r=(r_o + r_i)/2)
$t \leq 6$ mm	2.0 t	1.0 t	1.5 t
6 mm < $t \leq 10$ mm	2.5 t	1.5 t	2.0 t
10 mm < t	3.0 t	2.0 t	2.5 t

Nine loadings were considered: three simple ones (axial compression N, major-axis bending M_y and minor-axis bending M_z) and six complex ones (combinations of the previous three). Their stress parameters are identified by red circles in the Ψ_w- Ψ_f bi-dimensional space shown in Figure **7**(b). As was done for the straight-edge RHS members, results obtained with the two GBT-based numerical model variants were first compared for the members subjected to axial compression and uniaxial bending. These comparisons showed that excluding the non-Vlasov deformation modes from the analyses leads to a visible accuracy loss. Therefore, the results presented and discussed were obtained by means of the Variant 2 of the GBT-based numerical model (all deformation modes included in the analyses) – the inspection of the strain energy components, discussed ahead in the paper, sheds fresh light on the local buckling mechanics of the rounded-edge RHS members.

The second part this study (Section 4.6) presents preliminary findings regarding the influence of medium-to-large rounded corners (larger than those commonly found in practice) on the local buckling behavior of uniformly compressed SHS members. The members analyzed exhibit corner radii varying between the minimum and maximum geometrically possible values, *i.e.*, with ratios between the corner radius and the flange width varying between 0 and 0.5, which correspond to straight-edge SHS members and circular hollow section (CHS) members, respectively.

4.1 Comparison of the GBT-Based Numerical Model with other Methodologies

This section presents the comparison between the equivalent buckling coefficients obtained in this work, by means of the developed GBT-based model (Variant 2), and those yielded by other formulations and/or methods, namely (i) analytical formulae and (ii) current code provisions. Due to the simplified nature of some of the latter approaches, a meaningful comparison can only be made for uniformly compressed SHS tubes. The results presented concern the set of 100 uniformly compressed SHS members selected from the EN10219-Part 2 (CEN 2006b)) database.

Following the findings reported by Marsh (1997), equivalent local buckling coefficient concerning SHS tubes with small rounded corners may be obtained from

$$\overline{k_w}^{Marsh}=\overline{k_f}^{Marsh}=4+0.24\pi^2\left(1\text{-}\nu^2\right)\left(\frac{r}{t}\right)^4\left(\frac{b_f}{t}\right)^2 \quad , \quad (12)$$

where the influence of the rounded corners is quantified by the second term, dependent on the r/t and b_f/t ratios, and always leads to a buckling coefficient increase. Figure 8 plots, against b_f/t, the equivalent local buckling coefficients obtained in this work and yielded by Eq. (12), for three r/t ratios: 1.5, 2.0 and 2.5. The observation of this figure prompts the following remarks:

(i) First of all, it is noted that Eq. (12) invariably overestimates the buckling coefficients obtained in this work, even if the differences are small – this overestimation appears to decrease as r/t grows.

(ii) For r/t=2 and r/t=2.5, the two approaches yield buckling coefficients that grow as as b_f/t decreases. This is not true for r/t=1.5, as the buckling coefficients obtained in this work slightly decrease with b_f/r, unlike those yielded by Eq. (12).

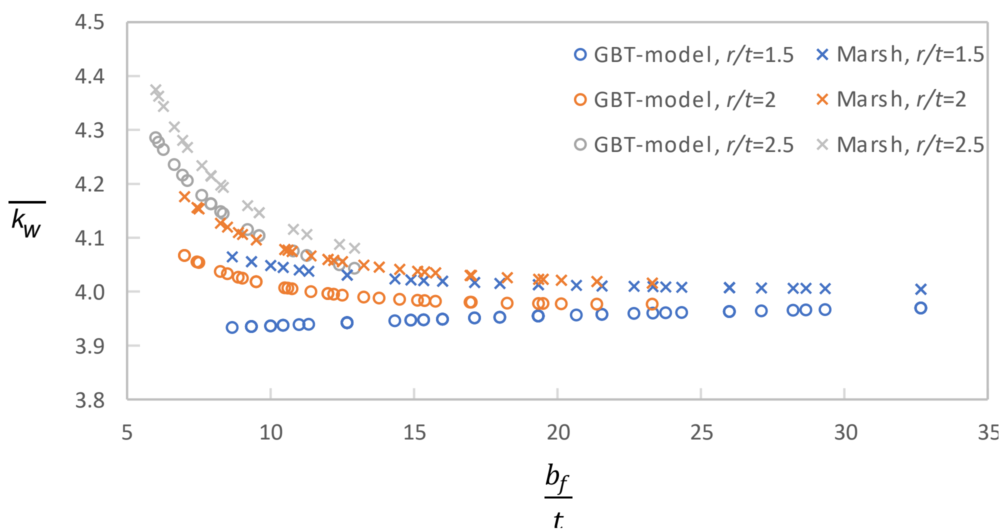

Figure 8: Comparison between the equivalent buckling coefficients obtained in this work and those due to Marsh (1997)

According to the "reduced k method" proposed in the Commentary to AISI (2016) (see Eq. 2), the equivalent buckling coefficients are calculated by means of

$$\overline{k_w}^{AISI\text{-}C}=\overline{k_f}^{AISI\text{-}C}=4\left(1.08\text{-}0.02\frac{r}{t}\right)^2\left(\frac{b_f}{b_f\text{-}2r}\right)^2\leq 4\left(\frac{b_f}{b_f\text{-}2r}\right)^2 \quad , \quad (13)$$

where $[b_f/(b_f-2\,r)]^2$ is the factor that "transforms" the buckling coefficients associated with the web flat width into the equivalent ones, associated with the distance between the flange mid-lines. Since the

r/t considered in this are all below 4 (see Table 4), the equivalent buckling coefficients are always computed as $4\times[b_f/(b_f-2r)]^2$, which leads to buckling coefficients much higher than those obtained in this work with the GBT-based model, as clearly depicted in Figure 9(a).

The results obtained with the GBT-based model are also considerably different from those yielded by the Eurocode 3 provisions (CEN 2006a), as shown in Figure 9(b). The latter state that the local buckling is to be handled by considering a reduced plate flat width equal to $b-2t$ (or $B-3t$, as specified in Eurocode 3 – B is the external width). Then, the expression providing the equivalent buckling coefficients becomes similar to the upper limit of Eq. (13) (with r replaced by t),

$$\overline{k_w}^{EC}=\overline{k_f}^{EC}=4\left(\frac{b_f}{b_f\text{-}2t}\right)^2 \quad . \tag{14}$$

As attested by the above comparisons, the North American and European specifications prescribe buckling coefficients that overestimate the (beneficial) influence of the rounded corners – they lead to local buckling loads much larger (up to 200%) than those obtained in this work.

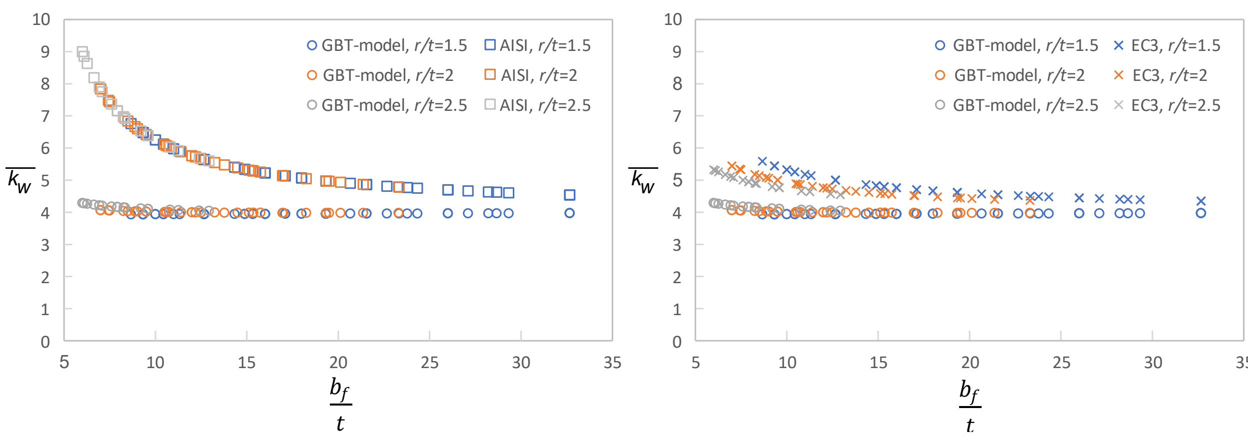

(a) (b)

Figure 9: Comparison between the equivalent buckling coefficients obtained in this work and those provided by the provisions of (a) AISI (2016) and (b) Eurocode 3 (CEN 2006a)

4.2 Illustrative Example

Before providing the whole set of results concerning the members exhibiting all the RHS selected from the EN10219-Part 2 (CEN 2006b) database, an in-depth study of members with a particular RHS and subjected to axial compression (loading case A), minor-axis bending (loading case C) or minor-axis bending (loading case G) is presented for illustrative purposes. An overall view of the illustrative RHS is given in Figure 10(a) and its dimensions are (in mm): external web height H=400, external flange width H=300, thickness t=12, mean corner radius r=30, mid-line web height h_w=$H-t$=388, mid-line flange width b_f=$B-t$=288, radial parameter $(h_w+b_f)/r$=22.5 and thickness parameter r/t=2.5. The main purpose of presenting these illustrative numerical results is to enable a better grasp of the changes in local buckling mechanics arising from the consideration of the rounded corners.

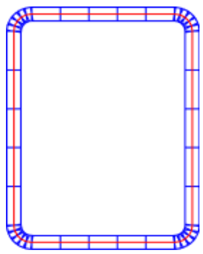

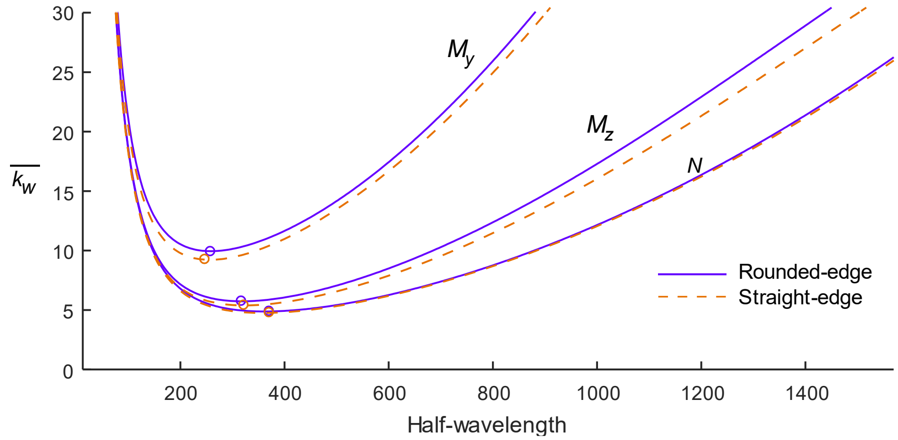

Figure 10: (a) Illustrative RHS geometry and discretization (5 elements per web, flange and corner) and (b) variations of the web buckling coefficient with the half-wave length for the rounded-edge and equivalent straight-edge configurations

Figure 10(b) shows the variations of the web buckling coefficient with the buckling mode longitudinal half-wave length for both the round-edge and equivalent straight-edge member configurations and the three loadings under consideration (the flange buckling coefficients exhibit identical variations). For the three loadings, both configurations lead to only one minimum within the small half-wave length range. This feature is well-known for the straight-edge configuration but not so for its rounded-edge counterpart – recall that, for instance, circular hollow sections, which constitute the SHS limit as the corner radii increase, exhibit a curve with several minima for axial compression (see Section 4.6). The above results show that the rounded corners lead to an increase in the minimum web buckling coefficient (between 3 and 8 percent in this particular case).

The buckling mode shapes and strain energy component percentages (with respect to the total strain energy U – recall Eqs. (7) and (8)) are provided in Figure 11. Concerning the straight-edge member, it is noted that the membrane energy percentages are practically null, which means that only Vlasov local deformation modes participate in the member buckling mode. It is also observed that there is very small cross-section warping in the straight-edge member under the three loadings – the warping displacements increase significantly in the presence of rounded corners (the highest values occur in their close vicinity). Moreover, the presence of rounded corners also leads to visible variations of some strain energy component percentages: the longitudinal and shear membrane ones (U_x^M and U_{xy}^M) increase, while the longitudinal and shear bending ones (U_x^B and U_{xy}^B) decrease. Overall, the membrane strain energy relevance increases by a few percent, at the expense of its bending counterpart.

It is also important to note that the highest $C_{k,r}$ value is not necessarily associated with the highest membrane strain energy percentage increase $\Delta U^M/U$ (Δ indicates the difference between the rounded-edge and straight-edge cases and $U^M = U_x^M + U_{xy}^M + U_y^M$), which can be confirmed by comparing the axial compression and minor-axis bending cases. However, it will be shown later that, within each loading case, there is some correlation between $\Delta U^M/U$ and $C_{k,r}$.

4.3 Local Buckling under Simple Loadings

This section presents the whole set of results obtained for the axial compression (Figure 12(a)-(d)), minor-axis bending (Figure 13(a)-(d)) and major-axis bending (Figure 14 (a)-(d)) cases, which show quite similar trends. The results concerning the rounded-edge member configurations are separated according to the *r*/*t* value. In each figure, the first plot includes (i) a curve providing the variation of the "exact" straight-

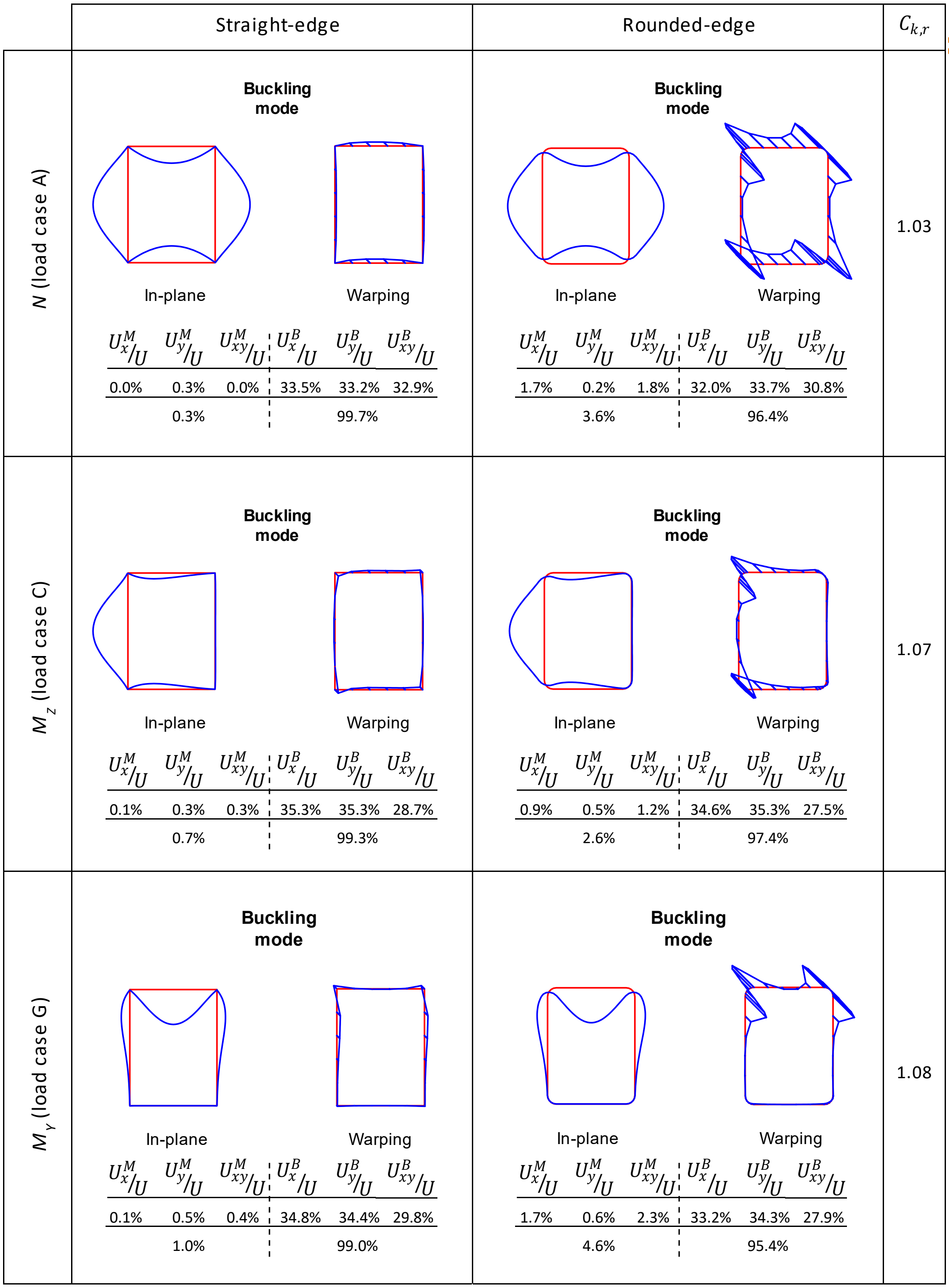

Figure 11: Buckling mode shapes, strain energy component percentages and $C_{k,r}$ values for the straight-edge and round-edge member configurations

edge member buckling coefficients with the h_w/b_f ratio and (ii) three sets of rounded-edge member equivalent buckling coefficients (each set concerns an r/t value considered: 1.5, 2.0 or 2.5). The above curve was obtained by means of a "curve fitting techniques" based on a very large number of local buckling results determined with the Variant 1 of the GBT-based model (small fractions of these results

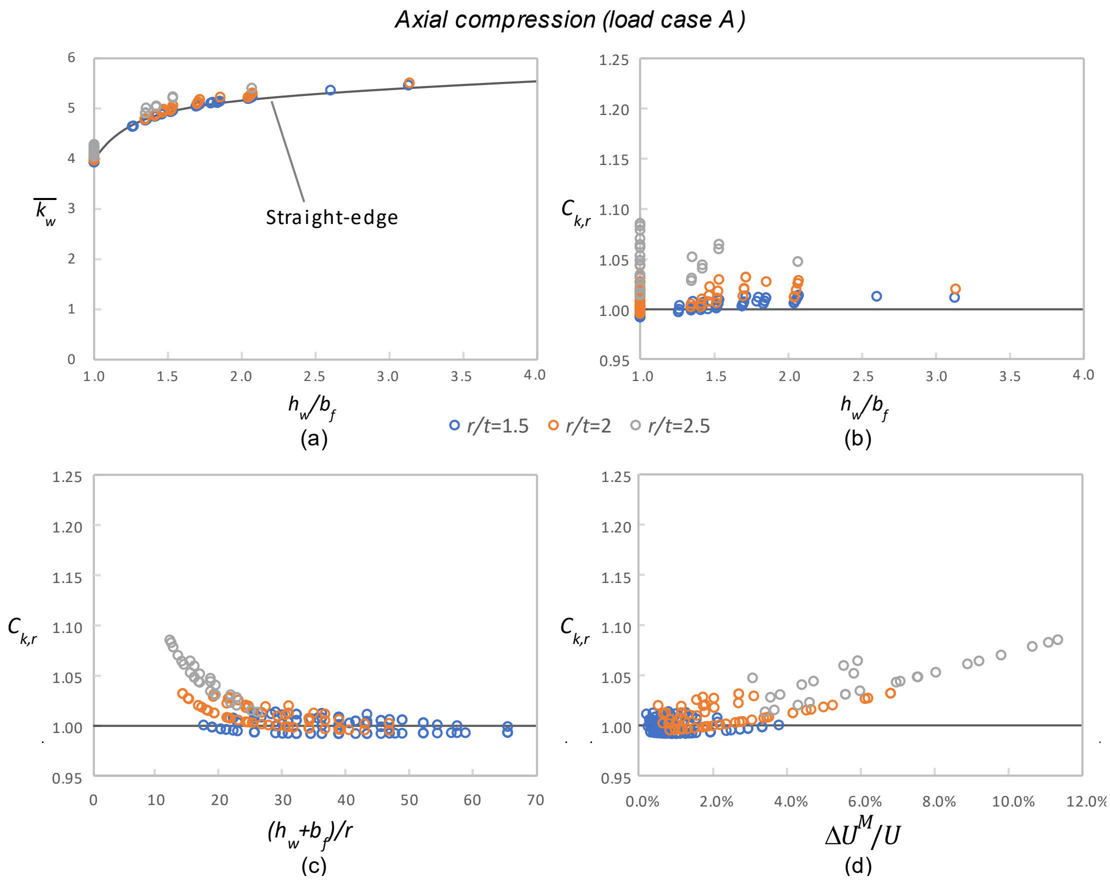

Figure 12: Plots (a) $\overline{k_w}$ vs. h_w/b_f, (b) and $C_{k,r}$ vs. h_w/b_f, (c) $C_{k,r}$ vs. $(h_w+b_f)/r$ and (d) $C_{k,r}$ vs. $\Delta U^M/U$ concerning the straight-edge and rounded-edge members under axial compression

were displayed in Figs. 2 to 4) and the rounded-edge member equivalent buckling coefficients were determined by means of Variant 2 of that same GBT-based model. As for the remaining three plots in the figures, they make it possible to visualize the $C_{k,r}$ value distribution expressed as a function of the (i) h_w/b_f ratio, (ii) radial parameter $(h_w+b_f)/r$ and (iii) membrane strain energy percentage increase $\Delta U^M/U$. Both the straight-edge member buckling coefficients (corresponding to the 1.0 horizontal lines) and the rounded-edge member equivalent buckling coefficients (providing the $C_{k,r}$ values) were obtained employing the Variant 2 of the GBT-based model.

The observation of the results presented in Figures 12(a)-(d) to 14(a)-(d) prompt the following remarks:

(i) Unlike in the straight-edge member case, it is no longer possible to express the equivalent buckling coefficients solely as a function of h_w/b_f for the rounded-edge members. Moreover, even if the effect of the wall thickness t must be taken into account, the r/t ratio still leads to a significant scatter. The above assertion can be clearly confirmed by looking at the plots $C_{k,r}$ vs. h_w/b_f, which show values ranging between about 1.0 and 1.2, but without exhibiting any clear trend regarding r/t – note that these plots also indicate that the presence of the rounded corners may increase the local buckling stresses up to 20%.

(ii) In the plots $C_{k,r}$ vs. $(h_w+b_f)/r$ (radial parameter) the rounded-edge member $C_{k,r}$ values concerning the three r/t ratios considered are more "packed together", thus providing some evidence of the existence of a "common trend". Moreover, as it would be logical to expect, $C_{k,r}$ tends asymptotically

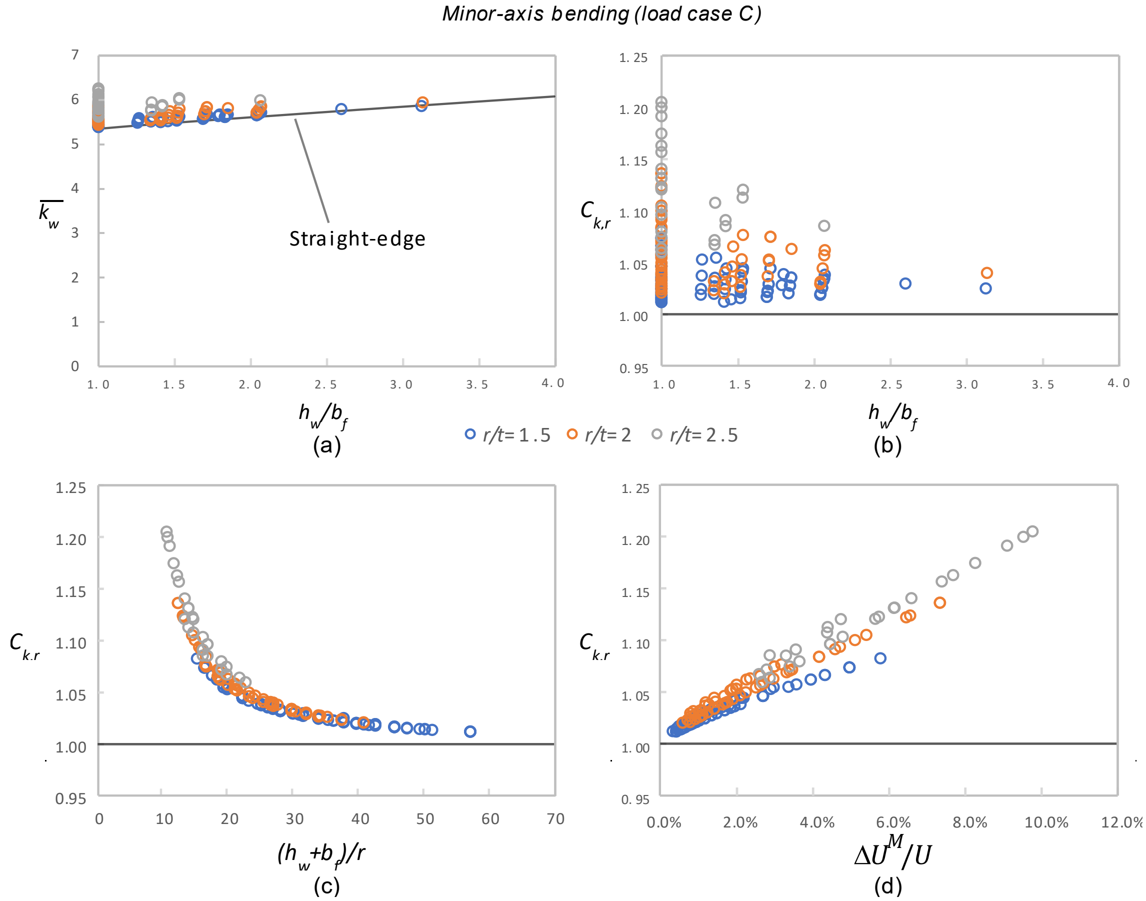

Figure 13: $\overline{k_w}$ vs. h_w/b_f, (b) and $C_{k,r}$ vs. h_w/b_f, (c) $C_{k,r}$ vs. $(h_w+b_f)/r$ and (d) $C_{k,r}$ vs. ΔU^M concerning the straight-edge and rounded-edge members under minor-axis bending

to the unit value as the corner radius progressively decreases. Conversely, a large corner radius leads to a $C_{k,r}$ value considerably above 1.0.

(iii) It is also worth noting that, within members sharing the same radial parameter, a thickness increase often leads to a larger $C_{k,r}$ value.

(iv) The plots $C_{k,r}$ vs. $\Delta U^M/U$ provide clear indications that there exist some correlation between the $C_{k,r}$ values and the membrane strain energy percentage increase, which suggests that the membrane action is linked to the improved local buckling behavior exhibited by the rounded-edge members – recall, from the illustrative example presented in Section 4.2, that the membrane energy increase stems almost exclusively from the growth of the strain energy component percentages U_x^M/U and U_{xy}^M/U, which are associated with the warping and shear effects.

(v) It is still worth mentioning that some of the $C_{k,r}$ values obtained are below 1.0 (particularly for the members under axial compression), which means that the presence of the rounded corners leads to a buckling coefficient decrease. Although the investigation of this surprising feature has already been initiated by the authors, it won't be addressed in this work, due to space limitations. The outcome of this ongoing study will be reported in the not too distant future.

4.4 Local Buckling under Combined Loading Cases

This section deals with the buckling behavior of RHS members subjected to various combinations of axial force and uniaxial or biaxial bending. A total of 2232 members were analyzed, corresponding to the

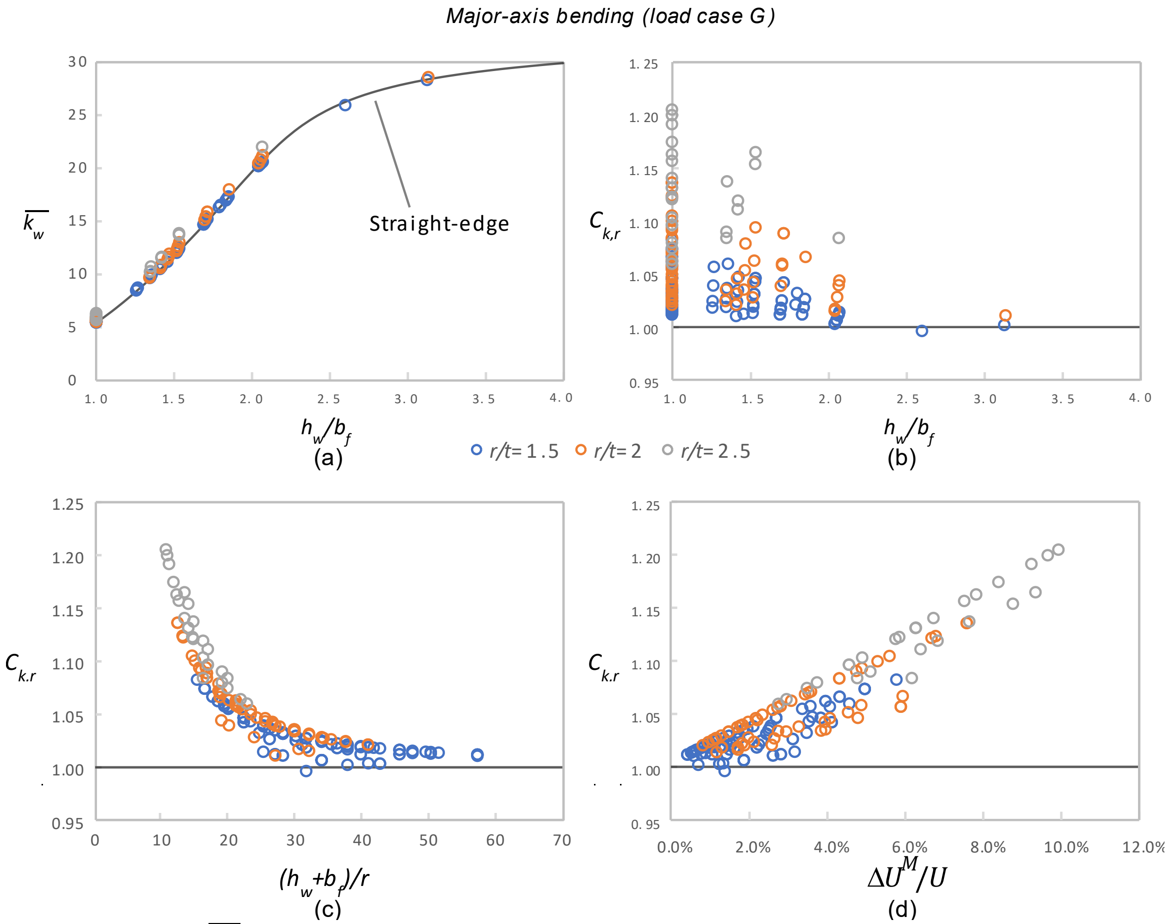

Figure 14: Plots (a) $\overline{k_w}$ vs. h_w/b_f, (b) and $C_{k,r}$ vs. h_w/b_f, (c) $C_{k,r}$ vs. $(h_w + b_f)/r$ and (d) $C_{k,r}$ vs. ΔU^M concerning the straight-edge and rounded-edge members under major-axis bending

loading cases B, D, E, F, H and I indicated in Figure 7(b). Since the results obtained are qualitatively similar to those presented and discussed in the previous sections, and due to space limitations, only a brief summary of the most relevant features is included in this paper – a much more detailed account can be found in a very recent work by the authors (Vieira *et al.* 2019). The following conclusions of the research effort carried out deserve to be specially highlighted:

(i) The presence of the rounded of corners generally leads to a bucking coefficient increase, which does not exhibit good correlation with the cross-section height-to-width ratio h_w/b_f – this is the main reason why no such results are presented in this paper.

(ii) A much better correlation can be obtained by plotting the $C_{k,r}$ ratios against the radial parameter $(h_w+b_f)/r$ – such plot makes it clear that a relative increase in the corner radius (*i.e.*, a decrease of the radial parameter) dimensions leads to higher equivalent buckling coefficient.

(iii) For similar radial parameter values, a wall thickness increase generally leads to higher $C_{k,r}$ values – this means that the influence of the rounded corners is generally higher in members with thick walls.

(iv) The $C_{k,r}$ ratio correlates positively with the difference between the membrane strain energy percentages of the rounded-edge and equivalent straight-edge RHS members – this difference stems mostly from warping and shear effects in the corner regions.

(v) In some RHS members with a r/t= 1.5, $C_{k,r}$ is below the unit value.

4.5 Approximate Formulae Accounting for the Rounded Corners

As mentioned previously (see Eq. (11)), $C_{k,r}$ is the ratio between the equivalent buckling coefficient determined for the rounded-edge member and the buckling coefficient obtained for the equivalent straight-edge member (both members share the same h_w and b_f values). Since analytical expressions have already been developed to calculate the straight-edge member buckling coefficients ($k_{w.str-edge}$ and $k_{f.str-edge}$), it now suffices to determine formulae to determine the $C_{k,r}$ ratio. The results presented in this work provide strong evidence that using "straight-edge buckling coefficients" (*i.e.*, assuming $C_{k,r}$ equal to 1.0) generally leads to safe local buckling loading predictions (*i.e.*, underestimations) – this is because such buckling coefficients are based on (fictitious) wider walls. Moreover, note that, in the few cases that do not follow the above general rule (*i.e.*, those for which the presence of rounded corners causes a buckling loading decrease), the buckling coefficient difference never exceeds 2%. Therefore, this section aims at presenting analytical expressions to calculate $C_{k,r}$. Although all the nine loadings cases identified earlier have been addressed, the expressions dealt with in this work concern only the simple loadings – expressions for the remaining loading cases can be found in Vieira *et al.* (2019).

It was decided to look for expressions based on the radial parameter $(h_w+b_f)/r$, since the numerical results indicated that it is a reasonable choice, even if a fair degree of scatter is still obtained. In order to achieve an adequate problem parameterization, the numerical results were split and curve-fitted according to the (i) the cross-section type (SHS or RHS), (ii) radius-to-thickness ratio r/t and (iii) loading case. The MATLAB (The MathWorks Inc. 2017) curve-fitting toolset was employed to develop the various analytical expressions. The best compromise between simplicity and accuracy was achieved with the expression

$$C_{k,r}=\frac{a}{\left(\frac{h_w+b_f}{r}-b\right)^2}+c. \quad , \quad (15)$$

where a, b and c are constants whose values are given in Table 5 for the simple loadings: axial compression (N), minor-axis bending (M_z) and major-axis bending (M_y). A very good fit is obtained, as shown in Figure 15, where the curves provided by Eq. (15) are compared with the numerical results – this is confirmed by the corresponding statistical indicators, not shown here (see Vieira *et al.* 2019).

4.6 Influence of Rounded Corner with Moderate-to-Large Radii – Preliminary Study

The previous sections addressed RHS member exhibiting rounded corners with radii commonly found in practice – such radii are almost always much smaller than the cross-section height and width: the ratio r/b_f varies between 0.03 and 0.17 (0.50 is the maximum possible). In order to extend the scope of this investigation beyond "rounded corners with small radii", this section addresses, for members under

Table 5: Values of the constants *a*, *b* and *c* appearing in the $C_{k,r}$ approximate analytical expression

		r/t=1.5			r/t=2.0			r/t=2.5		
	Loading	a	b	c	a	b	c	a	b	c
SHS	N	2.195	-0.001	0.991	8.042	-0.004	0.991	17.79	-1.668	0.990
	M_z	38.59	-4.862	1.004	39.30	-3.337	1.005	42.16	-2.607	1.008
	M_y	38.59	-4.862	1.004	39.30	-3.337	1.005	42.16	-2.607	1.008
RHS	N	229.7	-86.55	0.991	34.27	-10.74	0.992	17.45	-0.823	0.997
	M_z	42.31	-7.354	1.005	39.98	-5.074	1.006	41.32	-3.883	1.007
	M_y	28.92	-0.089	0.996	29.28	-0.054	1.003	39.94	-0.621	1.003

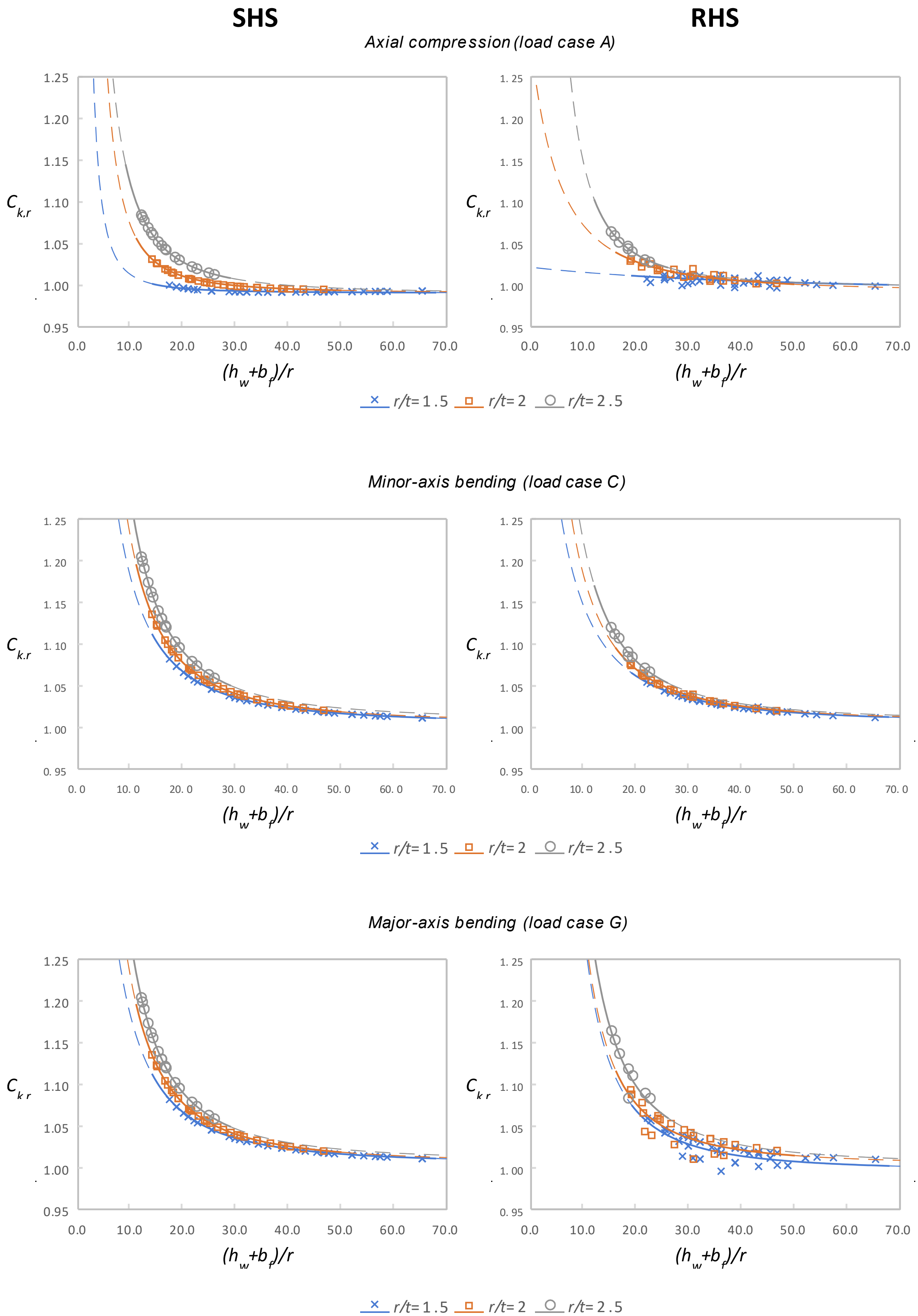

Figure 15: Curve-fitting of $C_{k,r}$ for SHS and RHS under the simple load cases A, C and G

axial compression, the influence of rounded corners with moderate-to-large radii on the local buckling behavior. In particular, insight on the local buckling mechanics is acquired for members with cross-sections covering the full range between straight-edge square (SHS) and circular (CHS) tubes.

The analyses were performed by means of the Variant 2 of the GBT-based numerical model and the all the cross-sections considered shared the dimensions h_w=b_f =100 mm and t=1 mm – the corner radius r varies between 0 (SHS) and 50 mm (CHS), in 1 mm steps. Following the outcome of a mesh sensitivity study, 10 wall segments were adopted in each corner, flange and web (such number was indispensable to analyze the members with cross-sections having r/b_f between 0.25 and 0.40). Figure 16 shows the variation of the equivalent web buckling coefficient with the half-wave length for members increasing corner radii (in 2 mm steps). The local minima of the various curves are identified by either a circle (lowest minima) or a small square (other minima).

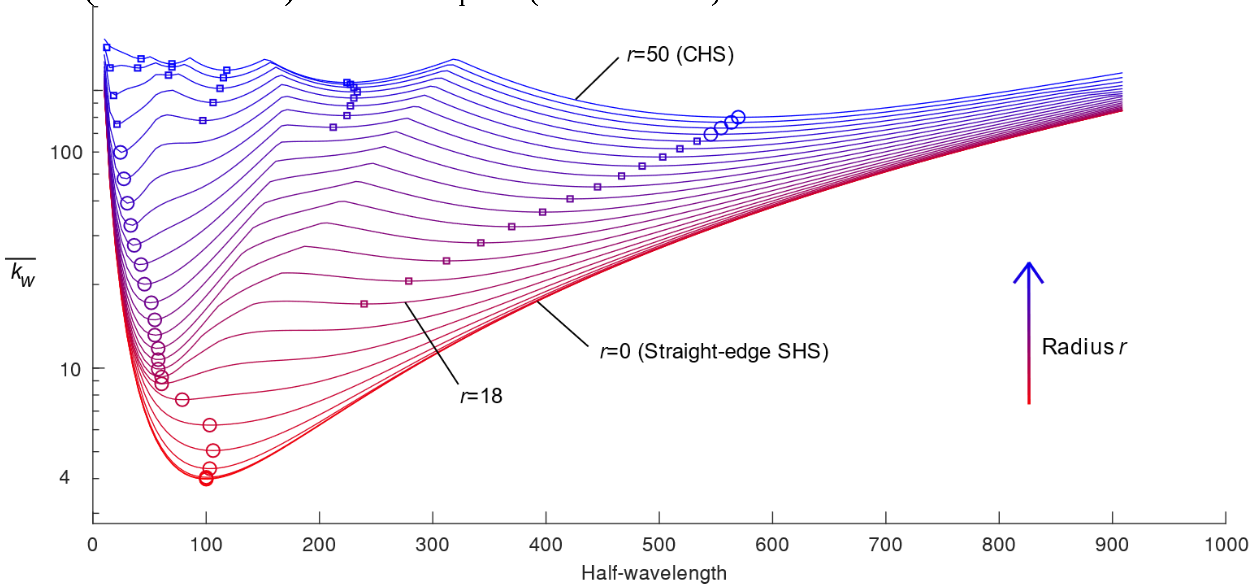

Figure 16: Variation of web buckling coefficient (logarithmic scale) with the half-wave length for uniformly compressed SHS members with h_w=b_f =100 mm, t=1 mm and r varying between 0 and 50 mm in 2 mm steps

Regarding the number of minima, it is observed that it increases as the cross-section approaches the CHS, even if a second minimum only occurs for corner radii equal or greater than 18 mm. As r increases, the lowest minimum buckling coefficient becomes substantially higher and corresponds to smaller half-wave lengths, except for cross-sections very close the CHS – in these cross-sections, the critical buckling mode is distortional. These observations are in good agreement with the results presented in Figure 17, which shows, for the various r values, (i) the strain energy component percentages, (ii) the minimum buckling coefficient and (iii) a few representative buckling mode shapes. As r increases, abrupt changes in the strain energy component percentages are observed – they stem from significant changes in buckling mode shape or nature. For corner radii up to 43 mm, the buckling modes are "local", since they involve much higher displacements in the flat walls than in the rounded corners, and are associated with larger contributions of the bending strain energy ($U^B = U_x^B + U_{xy}^B + U_y^B$) to the total strain energy. Indeed, the local buckling mode shape is (i) rotational anti-symmetric for $0 < r \leq 13$ mm, (ii) rotational symmetric, for $14 < r \leq 33$ mm, and (iii) rotational anti-symmetric for $34 < r \leq 43$ mm. For $r > 43$ mm, the critical buckling mode is distortional and involves almost solely longitudinal membrane (U_x^M) and transverse bending (U_y^B) strain energies.

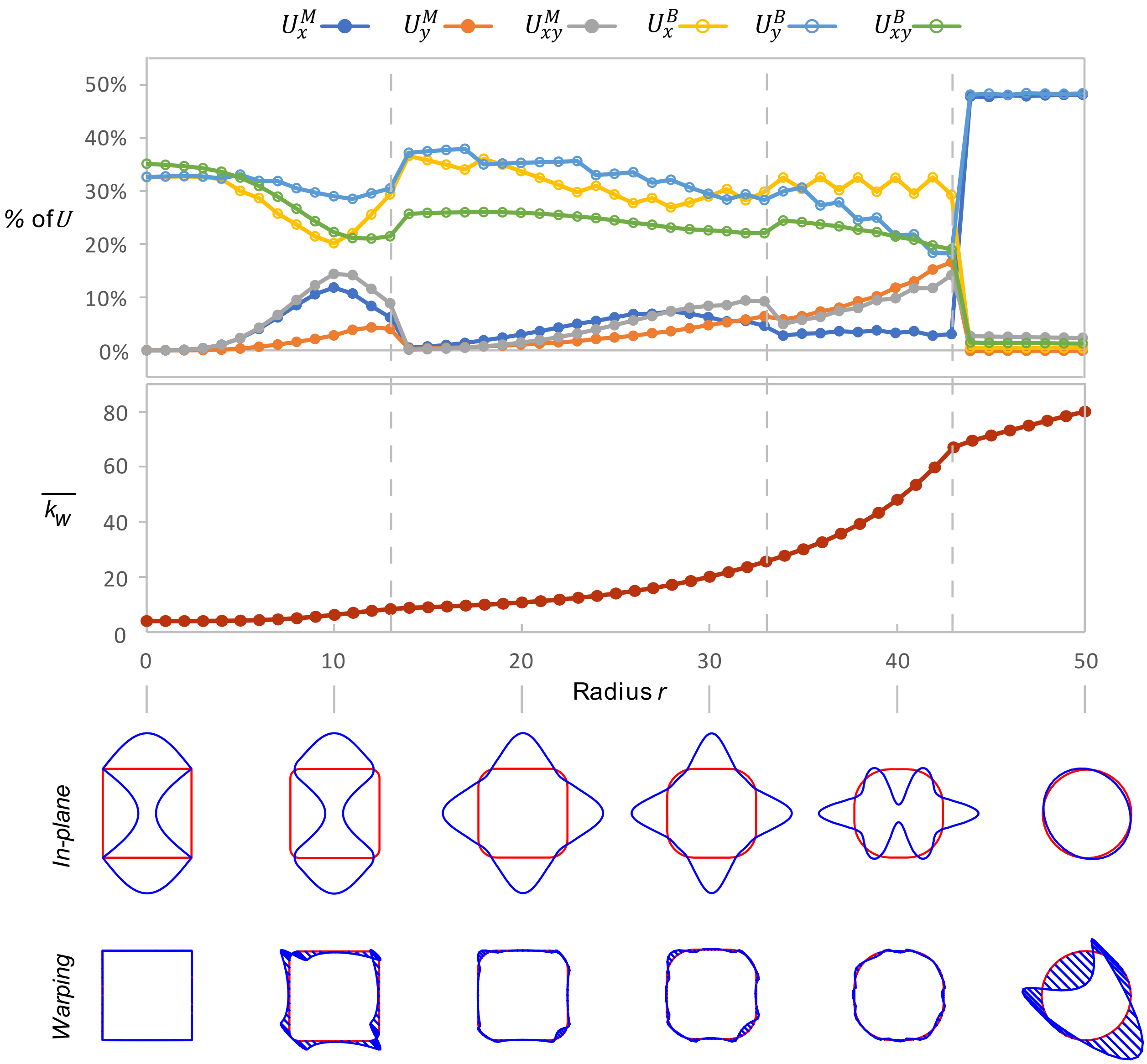

Figure 17: Strain energy component percentages, equivalent web buckling coefficients and buckling mode shapes of uniformly compressed SHS members with h_w=b_f =100 mm, t=1 mm and r varying between 0 and 50 mm in 1 mm steps

5. Conclusions

This paper reported results of an ongoing numerical study on the local buckling behavior of RHS members subjected to combinations of axial load and biaxial bending. The critical local buckling loads were calculated by means of a numerical model based on a computationally efficient GBT formulation specifically developed for RHS members. Both members with straight and rounded edges were analyzed. For straight-edge members, it was shown that the inclusion of only Vlasov local deformation modes in the GBT-based buckling analysis suffices to provide accurate local bifurcation loads for non-compact cross-sections. This fact made it possible to perform analyses that depend only on the cross-section (i) normal stress distribution and (ii) mid-line height-to-width ratio (h_w/b_f) – the results obtained with this model were shown to agree very well with those available in literature for either axial compression, major-axis bending or minor-axis bending (members subjected to combinations of axial force and biaxial bending were tackled for the first time by the authors). For each loading case, charts and approximate analytical expressions, obtained from curve-fitting techniques, were developed.

For rounded-edge members, it was showed that, in order to obtain accurate local buckling results, it is indispensable to included in the GBT-based buckling analysis also shear and transverse extension deformation modes. The results obtained provided solid evidence that the local buckling coefficients and loadings increase in the presence of rounded corners (except for a few cross-section with small radius-to-thickness ratios). It was concluded that the buckling coefficient/loading increase becomes more significant as the cross-section radius and thickness increase with respect to its mid-line height and width. Moreover, a correlation was found between this increase and the increase in the buckling mode linear membrane strain energy components associated with warping and shear.

For uniformly compressed square tubes with rounded edges, a comparison between the numerical results obtained in this work and those provided by the provisions of either Part 1-5 of Eurocode 3 or the North American Specification for the Design of Cold-Formed Steel Structural Elements of the showed that the last two often lead to unsafe local buckling loading predictions. Curve-fitting techniques were employed to develop approximate (but accurate) analytical expressions to calculate critical local buckling loadings of rounded-edge RHS members – they provide "correction factors" to be multiplied by the corresponding buckling loadings determined for equivalent straight-edge RHS members.

Finally, the influence of the presence rounded corners with medium-to-large radii on the local buckling behavior of uniformly compressed square tubes with (i) fixed web height, flange width and wall thickness, and (ii) different corner radii, whose variation covers the whole range between a straight-edge square tube and a circular hollow tube. It was shown, for this particular case, that (i) the equivalent web buckling coefficient increases with the corner radius and (ii) the critical buckling mode nature changes, from local to distortional, when the cross-section becomes quite close to a circular tube.

Acknowledgements

The authors gratefully acknowledge the financial support provided by the Research Fund for Coal and Steel (RFCS), through project RFCS-2015-709892 ("Overall-Slenderness Based Direct Design for Strength and Stability of Innovative Hollow Sections – HOLLOSSTAB").

References

AISI (American Iron and Steel Institute) (2016). *North American Specification (NAS) for the Design of Cold-Formed Steel Structural Members* (AISI-S100-16) + respective *Commentary*, Washington DC.

Bebiano R, Camotim D, Gonçalves R (2018). GBTUL 2.0 – A second-generation code for the GBT-based buckling and vibration analysis of thin-walled members, *Thin-Walled Structures*, **124**(March), 235-257.

CEN (Comité Européen de Normalisation) (2006a). *Eurocode 3: Design of Steel Structures – Part 1-5: Plated Structural Elements*, EN 1993-1-5:2006, Brussels, Belgium.

CEN (Comité Européen de Normalisation) (2006b). *Cold Formed Welded Structural Hollow Sections of Non-Alloy and Fine Grain Steels – Part 2: Tolerances, Dimensions and Sectional Properties*, European Standard EN 10219-2:2006, Brussels, Belgium..

Gonçalves R, Camotim D (2016). GBT deformation modes for curved thin-walled cross-sections based on a mid-line polygonal approximation, *Thin-Walled Structures*, **103**(June), 231-243.

Gonçalves R, Ritto-Corrêa M, Camotim D (2010). A new approach to the calculation of cross-section deformation modes in the framework of generalized beam theory, *Computational Mechanics*, **46**(5), 759-781.

Kiefer J (1953). Sequential minimax search for a maximum, *Proceedings of the American Mathematical Society*, **4**(3), 502-506.

Li Z, Schafer BW (2010). Buckling analysis of cold-formed steel members with general boundary conditions using CUFSM: conventional and constrained finite strip methods, *Proceedings of 20th International Specialty Conference on Recent Research and Developments Cold-Formed Steel Desiogn and Construction* (St. Louis, 3-4/11), R. LaBoube, W.-W. Yu (eds.), 17-31.

Marsh C (1997). Influence of bend radii on local buckling in cold formed shapes, *Journal of Structural Engineering* (ASCE), **123**(12), 1686-1689.

Schardt R (1989). *Verallgemeinerte Technische Biegetheorie*, Springer-Verlag, Berlin. (German)

Seif M., Schafer BW (2010). Local buckling of structural steel shapes, *Journal of Constructional Steel Research*, **66**(10), 1232-1247.

Stowell EZ, Lundquist EE (1939). *Local Instability of Columns with I, Z, Channel, and Rectangular-Tube Sections*, National Advisory Committee for Aeronautics (NACA) Technical Note (TN) 743, Washington DC.

The MathWorks Inc. (2017). MATLAB, Natick, Massachussets.

Vieira L, Gonçalves R, Camotim D (2018). On the local buckling of RHS members under axial force and biaxial bending, *Thin-Walled Structures*, **129**(February), 10-19.

Vieira L, Gonçalves R, Camotim D (2019). Influence of rounded corners on the local stability of RHS members under axial force and biaxial bending, *submitted for publication*.

Zeinoddini V, Schafer BW (2010). Impact of corner radius on cold-formed steel member strength, *Proceedings of 20th International Specialty Conference on Recent Research and Developments Cold-Formed Steel Desiogn and Construction* (St. Louis, 3-4/11), R. LaBoube, W.-W. Yu (eds.), 1-15.